IEEE Photonics Journal
An IEEE Photonics Society Publication

Slow-Light-Enhanced Silicon Optical Modulators Under Low-Drive-Voltage Operation

Volume 4, Number 5, October 2012

Antoine Brimont
Ana M. Gutierrez
Mariam Aamer
David J. Thomson
Frederic Y. Gardes
Jean-Marc Fedeli
Graham T. Reed
Javier Martí
Pablo Sanchis

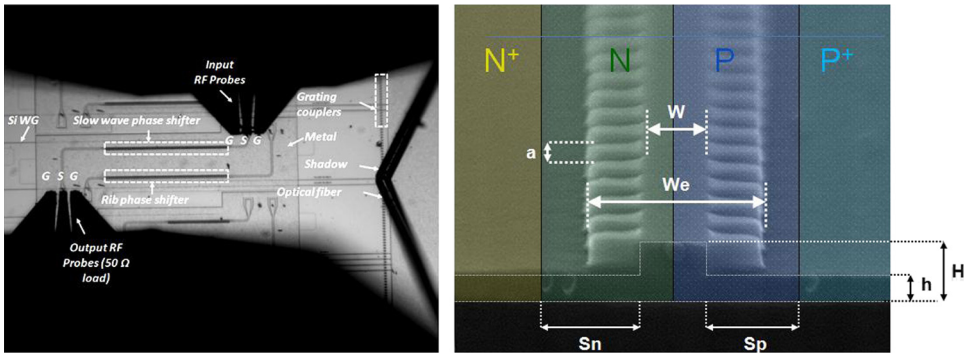

DOI: 10.1109/JPHOT.2012.2207884
1943-0655/$31.00 ©2012 IEEE

Slow-Light-Enhanced Silicon Optical Modulators Under Low-Drive-Voltage Operation

Antoine Brimont,[1] Ana M. Gutierrez,[1] Mariam Aamer,[1] David J. Thomson,[2] Frederic Y. Gardes,[2] Jean-Marc Fedeli,[3] Graham T. Reed,[2] Javier Martí,[1] and Pablo Sanchis[1]

[1]Nanophotonics Technology Center, Universitat Politècnica de València, 46022 Valencia, Spain
[2]School of Electronics and Computer Science, University of Southampton, SO17 1BJ Southampton, U.K.
[3]CEA, LETI, 38054 GRENOBLE Cedex, France

DOI: 10.1109/JPHOT.2012.2207884

Manuscript received April 24, 2012; revised June 29, 2012; accepted July 2, 2012. Date of current version July 25, 2012. This work was supported by the European Commission under Project HELIOS (photonics electronics functional integration on CMOS), FP7224312, and by the TEC2008-06333 SINADEC and PROMETEO-2010-087 R&D Excellency Program (NANOMET). The work of F. Y. Gardes, D. J. Thomson, and G. T. Reed was supported by the UK Environmental and Physical Sciences Research Council funding body under the grant "UK Silicon Photonics." Corresponding author: P. Sanchis (e-mail: pabsanki@ntc.upv.es).

Abstract: The integration of nanophotonics components with advanced complementary metal–oxide–semiconductor (CMOS) electronics requires drive voltages as low as 1 V for enabling next-generation CMOS electrophotonics transceivers. Slow-light propagation has been recently demonstrated as an effective mechanism to enhance the modulation efficiency in free-carrier-based electrooptical silicon modulators. Here, we exploit the use of slow light to reduce the driving voltage of carrier-depletion-based Mach–Zehnder modulators. The slow-light phase shifter consists of a p-n junction positioned in the middle of a corrugated waveguide. A modulation efficiency as high as $V_\pi L_\pi \sim 0.6$ V · cm is achieved, thus allowing data transmission rates up to 10 Gb/s with a 1.5-V_{pp} drive voltage and an insertion loss of ~12 dB. The influence of the drive voltage on the modulation speed as well as the variation of the insertion losses with a group index is also analyzed and discussed.

Index Terms: Slow light, photonic band-gap structures, silicon nanophotonics, optical interconnects.

1. Introduction

The ability to slow down the velocity of light has been foreseen as a very useful mechanism for enhancing performances in numerous applications ranging from telecom and datacom to sensing via enlarged light–matter interactions [1]–[4]. In particular, slow light achieved by means of nanostructured periodic waveguides has been demonstrated as an effective mechanism for pushing forward the limits of nonlinear and free-carrier-based electrooptical phenomena in silicon [5]–[8].

In the last decade, free-carrier-based electrooptical silicon modulators have been the subject of a growing interest since they are key building blocks for enabling next-generation complementary metal–oxide–semiconductor (CMOS) electrophotonics transceivers in silicon photonics technology. Initially, developing a fast modulator was the challenge to be overcome. The first silicon modulator exceeding a 1-GHz bandwidth was demonstrated in 2004 [10]. Less than a decade later, data rates up to 50 Gb/s have been achieved in pure silicon [9]. However, in recent years, the race has been

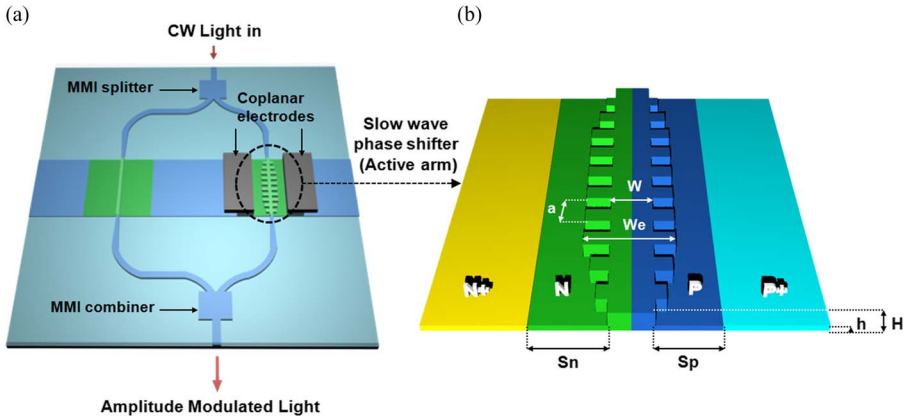

Fig. 1. (a) Schematic of the modulator based on an asymmetric MZI. Multimode interference (MMI) structures are used to split and combine the light, respectively, at the input and output of the MZI. (b) Close-up view of the slow-light phase shifter.

mainly focused on minimizing the drive voltage to meet the stringent values required for monolithic integration with CMOS transistors, which can currently supply about 1.2 V_{pp}.

The use of microring resonators was originally demonstrated as a means to decrease the drive voltage down to 1 V_{pp} without altering the speed performance of the modulator (12.5 Gb/s) [11]. Further research on low-voltage microring resonators showed that high-speed operation (30 Gb/s) is achievable while sustaining the drive voltage around 1.6 V_{pp} [12]. Additionally, a microring resonator embedded into interleaved p-n junctions has enabled a 25-Gb/s data rate with 2 V_{pp} [13]. Very recently, low-voltage operation (3.5 V_{pp}) allowing a full pi-phase shift has been also demonstrated in Mach–Zehnder interferometer (MZI) modulators but at the expense of large footprints (6-mm-long phase shifters) [14]. To further decrease the drive voltage, MZI modulators operated in differential mode (or push pull) featured a transmission rate up to 30 Gb/s with 1.2 V_{pp} in a 1-mm-long phase shifter [15]. More recently, 26-Gb/s operation has been shown with a differential voltage as small as 0.5 V [16]. In this paper, we take advantage of the high modulation efficiency achievable in slow-light modulators in order to lower the drive voltage down to values that fulfill current CMOS requirements. As a result, a relatively compact single-drive 1-mm-long phase shifter featuring low drive voltage, moderate insertion loss, and high-speed performance is demonstrated.

2. Device Description and Fabrication

Fig. 1(a) and (b) shows the schematic of the designed slow-light modulator as well as a close-up view of the slow-light phase shifter. Slow light interacting with the variable concentration of free carriers is the effect intended to be used as a means to increase light–matter interactions, thus enhancing the modulation efficiency. Optical phase modulation in the slow-light waveguide is converted into amplitude modulation via the use of an asymmetric MZI. One arm of the MZI consists of a 1-mm-long slow-light phase shifter, whereas the other arm contains a rib waveguide having the same length and doping conditions.

Slow-light propagation is achieved through the use of a laterally corrugated waveguide (LCWG), with narrow and wide sections of width $W = 300$ nm and $We = 650$ nm, which are repeated over a period $a = 310$ nm, as shown in Fig. 1(a) and (b). The slow-light waveguide height is 220 nm, which, after partial dry etching process, leaves a 100-nm-thick slab. Optical phase modulation is achieved by depleting the majority carriers from a reverse-biased p-n junction positioned in the middle of the waveguide and connected to highly doped p^+ and n^+ regions. These are situated, respectively, at a distance of $Sn = 550$ nm and $Sp = 500$ nm from the edge of the narrow waveguide section and covered with compound AlCu electrodes in order to ensure good ohmic contacts. Net doping concentrations in the p- and n-type regions reached 4.10^{17} at/cm^{-3} and 5.10^{17} at/cm^{-3}, respectively. Highly p^+- and n^+-doped regions were implanted both at a concentration of 1.10^{20} at/cm^{-3}.

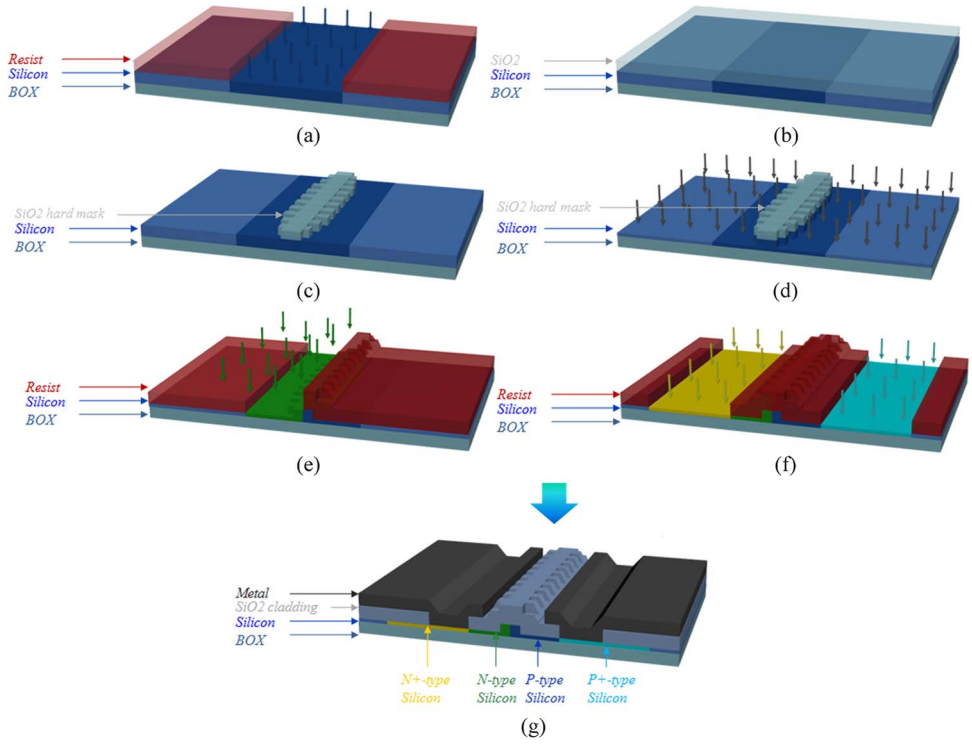

Fig. 2. CMOS fabrication process of the slow-light modulator.

For completeness, the required standard CMOS fabrication steps to realize the slow-light modulators are summarized in Fig. 2. The process starts with a) light p-type implantation, through positive resist window opening in a 220-nm-thick silicon layer on top of a 2-μm-thick buried oxide layer (BOX). This forms the p-type background. b) Then, the resist is removed (stripping), and a SiO_2 layer is deposited. c) Next, a lithographic step followed by an etching is performed to define the waveguide SiO_2 hard mask. d) The 220-nm-thick silicon layer is then partially etched down to leave a 100-nm-thick slab. e) The SiO_2 hard mask on top of the waveguide is then stripped, and the edge of the resist windows is positioned in the middle of the waveguide. The resist layer window opening enables the positioning of the n-type implantation area from the middle of the waveguide. f) Then, p^+-type and n^+-type implantation are carried out separately through lithography and photoresist window opening. Dopant electrical activation is performed through rapid thermal annealing (RTA) (1050 °C for 10 s). g) Finally, the device is covered with a SiO_2 upper cladding, and windows are opened on the p^+ and n^+-type region. A metal layer is then deposited on top and etched to form ohmic contacting electrodes.

Fig. 3(a) and (b) shows an optical microscope image of the slow-light modulator under test as well as a close-up SEM image of the fabricated corrugated waveguide. As can be observed from Fig. 3(a), the incoming coherent light is coupled vertically to the chip via grating couplers. A traveling-wave ground–signal–ground (GSG) coplanar design has been used to enable further high-speed radio-frequency measurements. Fig. 3(b) shows the slow-light waveguide parameters. Doping regions are delimited by the colored areas.

3. Slow-Light Modulator Performance

3.1. Insertion Loss and Group Index

A simple method is proposed to accurately measure the insertion losses of the slow-light phase shifter. In order to estimate the insertion losses versus group index with a single measure, the method exploits the MZI structure consisting of a slow-light waveguide in one of its arms, as

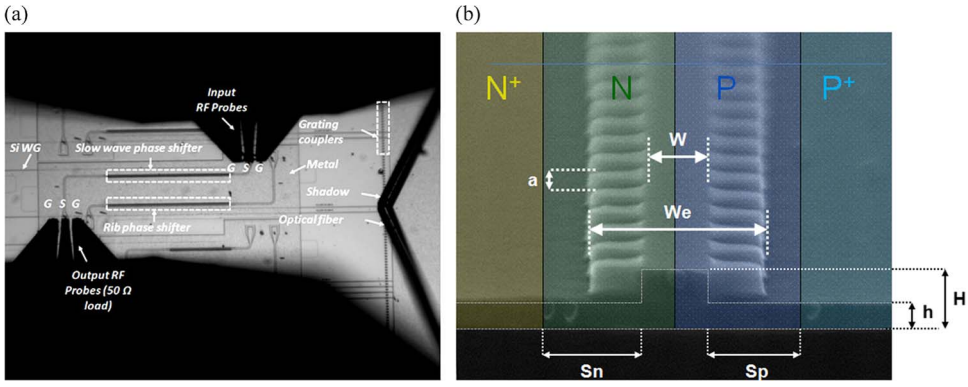

Fig. 3. (a) Optical microscope image of the slow-light modulator under test. (b) Perspective front view of the corrugated waveguide (scanning electron microscope). Doping regions are delimited by the colored area.

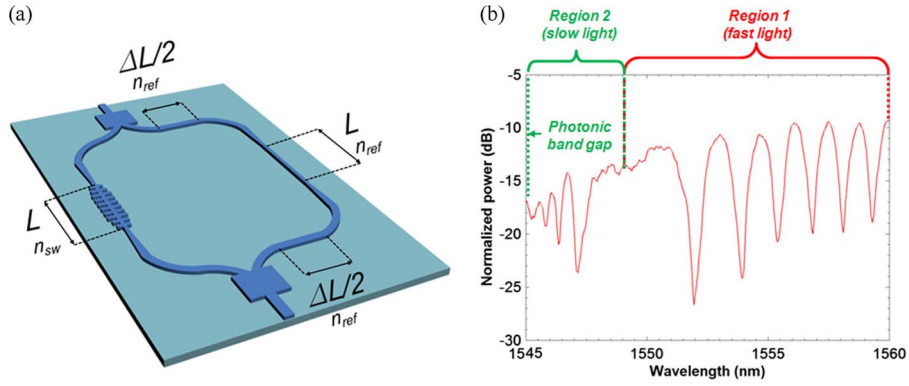

Fig. 4. (a) Schematic of the MZI structure used in the proposed method to estimate the insertion losses in the slow-light phase shifter. (b) Normalized optical transmission spectrum of the MZI structure.

illustrated in Fig. 4(a). It should be noticed that the calculation of the group index variations has been proposed with similar procedures [17], [18]; however, to the best of our knowledge, a method for also estimating the insertion losses from the MZI spectrum has not yet been reported.

Fig. 4(b) shows the optical transmission spectrum of the MZI structure. The free spectral range (FSR) changes across the spectrum as a result of the group index dependence upon wavelength, which increases as we approach the band edge of the slow-light mode. Therefore, the FSR variations across wavelength can be used to extract the group index from

$$\mathrm{FSR}(\lambda) \approx \frac{\lambda^2}{n \cdot \Delta L + (n_{ref} \pm n_{sw}(\lambda)) \cdot L} \tag{1}$$

where λ is the central wavelength of the FSR; n_{sw}, n_{ref}, and n are the respective group indices in the slow-light, 300-nm-wide reference rib, and 400-nm-wide rib waveguides; L is the length of the slow-light and reference rib waveguides, which is the same; and ΔL stands for the length difference between the MZI arms considering only the 400-nm-wide rib waveguide. In our case, $L = 1$ mm, $\Delta L = 0.9$ mm, $n_{ref} \approx 3.5$, and $n \approx 3.7$. The selection of the sign in the right-hand side of (1) depends upon the considered wavelength range and is related to the fact that the FSR exhibits different behaviors as we move from the fast-light region toward the photonic band gap (PBG), as can be observed in Fig. 4(b).

In the fast-light regime (far enough from the PBG), the separation between the interference fringes remains approximately constant, which is consistent with a nearly unvarying group index

value, and the negative sign must be used in (1). However, as we enter the slow-light regime, i.e., as we move closer to PBG, the FSR increases up to a maximum value, which means that the phase difference between the MZI arms is minimized. According to (1), the FSR is infinite when the denominator is zero, which means that there is no phase difference between the MZI arms. It can be straightforwardly obtained that this occurs for a group index of 6.8. From this point forward, the positive sign must be used in (1) because higher group indices imply that the effective optical path length of the shorter arm becomes larger than that of the longer arm, thus causing the FSR to decrease.

The influence of loss variations versus group index in the slow-light waveguide is also clearly observed in Fig. 4(b). Initially, the losses in the reference arm are higher than in the fast-light region (i.e., the region where the group index is approximately constant) of the slow-light waveguide, hence reducing the contrast ratio of the MZI interference fringes. As the group index increases, the losses in the slow-light waveguide increase accordingly, reducing further the power imbalance between arms. This, in turn, contributes to improve the contrast ratio. The maximum contrast ratio is achieved when the total losses in each of the MZI arms are similar, which takes place for wavelengths around 1552 nm. At wavelengths lower than 1552 nm, the power imbalance increases back again, reducing therefore the contrast ratio, though this time caused by higher losses in the slow-light waveguide. Therefore, the insertion losses in the slow-light phase shifter can be estimated from the variation of the contrast ratio with wavelength. The proposed method for estimating the insertion losses starts from the evaluation of the maximum and minimum electrical field at the MZI output, which can be written as

$$E_{\max}(\lambda) = E_0\left(m_L \cdot c_p(\lambda) \cdot e^{-\alpha_{sw}(\lambda)L} + m_{L+\Delta L} \cdot e^{-(\alpha_{ref}L+\alpha\Delta L)}\right) \tag{2}$$

$$E_{\min}(\lambda) = E_0\left(m_L \cdot c_p(\lambda) \cdot e^{-\alpha_{sw}(\lambda)L} - m_{L+\Delta L} \cdot e^{-(\alpha_{ref}L+\alpha\Delta L)}\right) \tag{3}$$

where E_o is an amplitude factor that includes the fiber-to-the-chip coupling losses; m_L and $m_{L+\Delta L}$ is the power branching coefficient of the splitter and combiner (it is assumed that both are identical); c_p accounts for the input and output coupling losses between the slow-light and rib waveguides; and α_{sw}, α_{ref}, and α are the respective propagation losses in nepers per unit length in the slow-light, reference rib, and rib waveguides. It is assumed that the propagation losses in the rib waveguides are approximately constant with wavelength. The following relation is obtained by combining (2) and (3)

$$E(\lambda) = 20\log_{10}\left(\frac{E_{\max}(\lambda)+E_{\min}(\lambda)}{E_{\max}(\lambda)-E_{\min}(\lambda)}\right) = Cte + C_p(\lambda) + (\alpha_{ref} - \alpha_{sw}(\lambda))L \tag{4}$$

where *Cte* is a constant value, which depends only on the possible splitter/combiner branching asymmetry and the $\alpha\Delta L$ losses. Thereby, we can obtain an estimation of both coupling and propagation losses within the slow-light waveguide at a given wavelength just by considering the maxima and minima or, in other words, the contrast ratio of the MZI interference fringes, which makes the proposed method independent on the external alignment and the fiber-to-the-chip coupling losses.

The insertion losses, which include both coupling and propagation losses, can be derived as follows

$$IL(\lambda) = C_p(\lambda) + \alpha_{sw}(\lambda)L \approx \alpha_{fw}L + \begin{cases} \overline{E} - E(\lambda), & \text{Region 1} \\ \overline{E} + E(\lambda), & \text{Region 2} \end{cases} \tag{5}$$

where α_{fw} and $\bar{E}$ are, respectively, the propagation losses and mean value of $E(\lambda)$ in the fast-light region, where the group index is approximately constant and where the coupling losses are assumed to be negligible. The two different expressions for regions 1 and 2 depicted in Fig. 4(b) assume that, in region 1, the output power from the longer arm is lower than that from the shorter arm, and vice versa in region 2, where the sign must be changed in (3) as also occurs in (1). The propagation losses, α_{fw}, can be estimated from (4) giving rise to a value around 3 dB/mm.

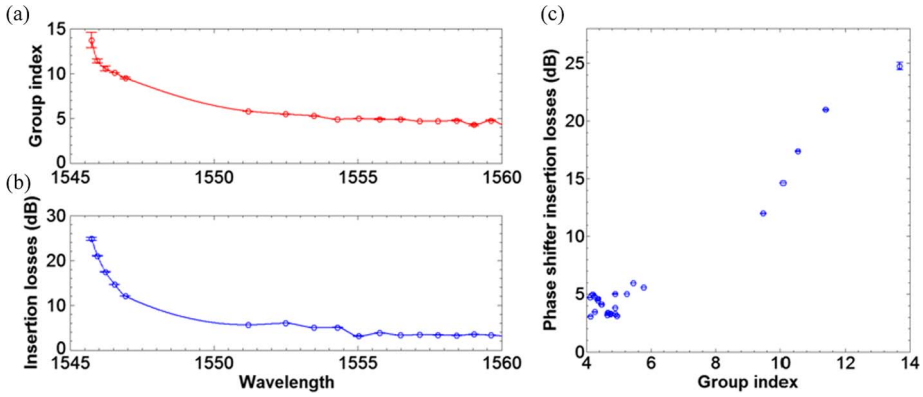

Fig. 5. (a) Group index and (b) insertion losses variation versus wavelength. (c) Slow-light phase shifter insertion loss versus group index.

Fig. 5 shows (a) the group index and (b) insertion loss dependence on wavelength, which are derived from (1) and (5), respectively. Both results can be combined in order to obtain the insertion losses versus group index of the slow-light phase shifter structure, as depicted in Fig. 5(c). It can be seen that the insertion losses increase for increasing group index, yielding to a tradeoff between high modulation efficiency and low insertion losses [7].

The increase in loss is partly attributed to the higher free-carrier-based absorption arising from the enhanced light–matter interaction. In fact, the insertion losses in the fast-light region are similar to those reported in other works with similar doping concentrations [15], [16]. Nevertheless, insertion losses as low as $\sim$2 dB for a group index of $\sim$28 have been reported in an MZI modulator with 200-μm-long slow-light phase shifters based on a 2-D photonic crystal structure although considering lower implantation doses [19]. Overall, strategies to reduce the insertion losses should be focused on optimizing the overlap between the active region and the slow-light mode propagating through the periodic optical waveguide. As a matter of fact, a doping compensation method in which the doping profile is optimized to reduce absorption losses without degrading the modulation efficiency and speed has been recently proposed and demonstrated for conventional silicon modulators [20]. Such a method could also be applied for the proposed slow-light modulator. Finally, improving the coupling technique to the slow-light mode would also be especially desirable as the group index increases.

3.2. Modulation Efficiency

The optical phase modulation in the slow-light waveguide is converted into amplitude modulation through the use of the asymmetric MZI. Fig. 6(a) shows the MZI slow-light modulator spectra under varying reverse-bias voltage. The bias voltage is varied between $+0.5$ and -2.5 V. Because the threshold voltage of this p-n junction is around $+0.8$ V (forward-bias operation), no current flow through the junction takes place under a $+0.5$-V bias voltage. This means that high-speed operation will not be limited by the free-carrier recombination time. The modulation efficiency increases with the group index, but using higher group indices will also have a negative impact on the insertion losses, as previously illustrated in Fig. 5(c). Nevertheless, a fairly low insertion loss of 12 dB has been measured for a moderate group index value of $\sim$9.5 at 1546.9-nm wavelength, which corresponds to the quadrature point indicated in Fig. 6(b).

Fig. 6(b) shows the experimental and simulated effective index change and modulation efficiency for varying reverse-bias voltage at the quadrature point. As can be observed, the modulation efficiency varies strongly for increasing reverse-bias voltage due to the nonlinear behavior of the p-n junction. Modulation efficiencies $V_\pi L_\pi$ as low as 0.42, 0.55, 0.62, 0.7, and 0.8 V $\cdot$ cm have been respectively extracted for 0.5, 1, 1.5, 2, and 3 V applied voltages at 1546.9-nm wavelength. Interestingly and in agreement with previous works [11], [13], [16], the p-n junction is clearly more efficient for lower reverse-bias variation. Although for bias voltage beyond -0.5 V both experimental

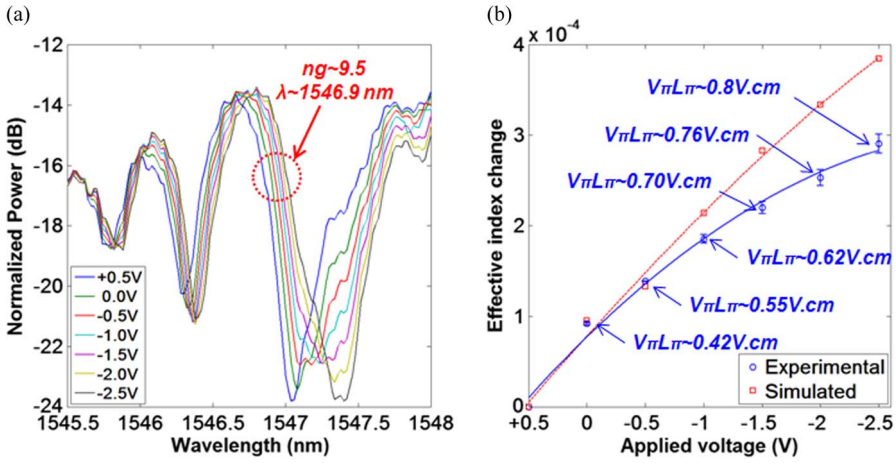

Fig. 6. (a) Close-up view of the slow-light region for bias voltages varying from +0.5 to −2.5 V. The dotted circle designated by the red arrow is the quadrature point. (b) Experimental (blue plain line) and simulated (red dashed line) effective index change versus applied voltages varying from +0.5 to −2.5 V at 1546.9-nm wavelength (measured at the quadrature point). Measured modulation efficiencies $(V_\pi L_\pi)$ for each corresponding applied voltage and taking +0.5 V as a reference are also shown.

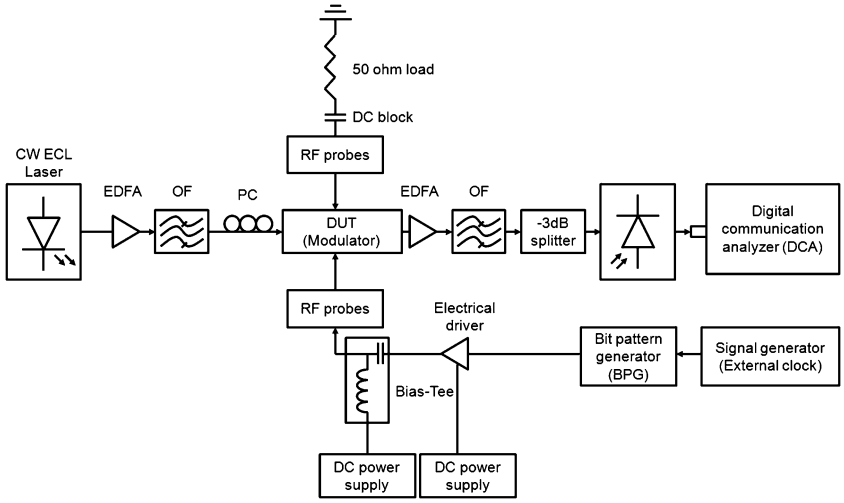

Fig. 7. Schematic of the characterization setup for dynamic measurements.

and simulated effective index changes are in good agreement, a slight discrepancy takes place below −0.5 V. We believe this might be due to the fact that we assume an ideal uniform doping profile in our electrical simulations, on one hand, and/or that the actual target doping concentrations are slightly lower than expected [21], on the other hand. One might also put forward the fact that the slow mode distribution might be altered from the plane-wave expansion simulations to experiment, hence interacting in a slightly less efficient way with charge carriers.

3.3. Dynamic Performance

A schematic of the high-speed characterization setup is shown in Fig. 7. Data transmission measurements were realized by driving the modulator with a nonreturn-to-zero (NRZ) pseudorandom bit sequence (PRBS) of length $2^{31} - 1$ delivered by a bit pattern generator (BPG), which is connected to an external clock. The electrical signal is amplified through a high-speed RF amplifier to achieve the desired voltage swing (V_{pp}) and combined to a dc bias using a bias-tee. Lower

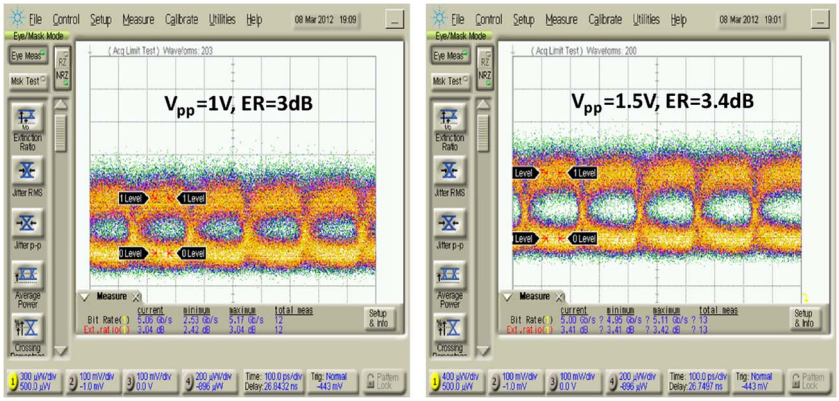

Fig. 8. Eye diagrams at 5 Gb/s for varying peak-to-peak drive voltage.

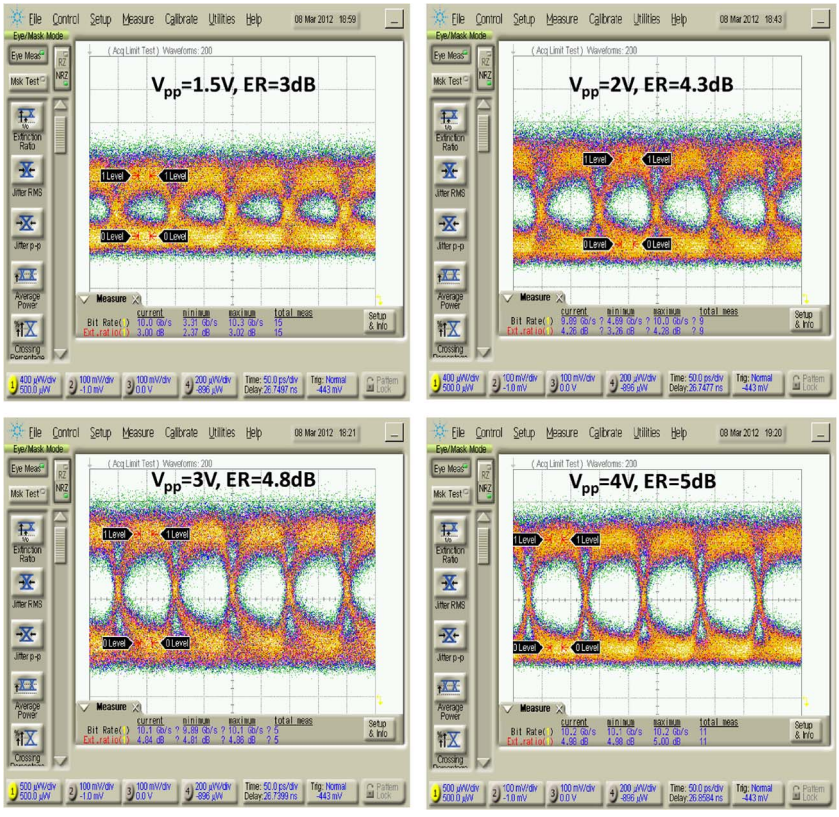

Fig. 9. Eye diagrams at 10 Gb/s for varying peak-to-peak drive voltage.

output voltages are achieved via a combination of attenuating the input signal delivered by the BPG to the RF amplifier and using the gain control function. The modulating signal is applied to the traveling-wave electrodes, which are terminated externally by a 50-Ω load coupled to a dc block. The output modulated optical signal is then filtered via an optical filter (OF), split equally (-3 dB) and photodetected by a digital communication analyzer.

To analyze the high-speed performance of the slow-light modulator under low drive voltages, eye diagram acquisitions at quadrature ($\lambda = 1546.9$ nm) from 5 to 25 Gb/s were carried out under drive voltage ranging from 1 to 4 V. The results are summarized in Figs. 8–10. Interestingly, and as a

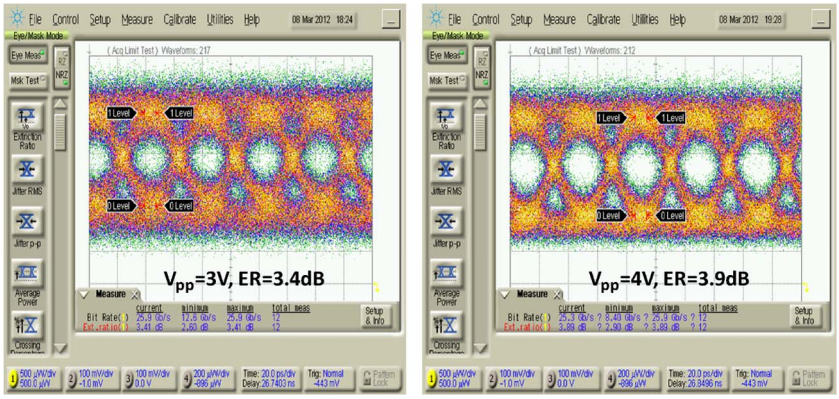

Fig. 10. Eye diagrams at 25 Gb/s for varying peak-to-peak drive voltage.

result of the high modulation efficiencies, the eye diagram in the range 5–10 Gb/s remains open for very low drive voltages (1, 1.5, and 2 V), and the corresponding extinction ratios lie between 3–4.3 dB. DC biases are 0, 0.25, and 0.5 V, respectively.

For drive voltages ranging from 3 to 4 V (respective dc biases are 1 and 1.5 V), the eye diagrams open up, showing that ultrahigh-speed operation at 25 Gb/s is achieved, as shown in Fig. 10. The relatively low extinction ratios are due to the power unbalance between the two arms of the MZI, which produces a null height of only 10 dB. Using an asymmetric MZI featuring two identical corrugated waveguides in each arm would increase the null height and lower the "0" level. This would notably increase the dynamic extinction ratios for drive voltage beyond 2 V.

4. Conclusion

The performance of a 1-mm-long slow-light modulator has been analyzed in terms of insertion loss, modulation efficiency, and dynamic operation under low drive voltages. The high modulation efficiency (0.55 V · cm for a 1-V swing) provided by the slow-light phase shifter with the p-n junction positioned in the middle of the waveguide allowed data transmission rates from 5 Gb/s with 1 V_{pp} up to 25 Gb/s with 3 V_{pp} with an insertion loss of $\sim$12 dB. Enhanced performance (higher extinction ratio) is expected when driving the modulator in push–pull while sustaining low drive voltages.

Moreover, a simple method has also been proposed for experimentally estimating the insertion losses versus group index of a slow-light photonic waveguiding structure. Only a single measure is required, and the loss estimation is independent of the alignment and fiber-to-the-chip coupling losses. The tradeoff between high modulation efficiency and low insertion losses, which relies on the group index operating point, has also been discussed. Furthermore, the perspective of using engineered slow-light structures to achieve broader optical bandwidths [22] leaves room for further improvements.

In summary, the promising combination of high modulation efficiency, low drive voltage, relatively low insertion loss, compactness, and high-speed operation gives all the more reasons for slow-light modulators to be used in more complex silicon photonic systems.

References

[1] T. Krauss, "Why do we need slow light?" *Nature Photon.*, vol. 2, no. 8, pp. 448–450, Aug. 2008.
[2] T. Baba, "Slow light in photonic crystals," *Nature Photon.*, vol. 2, no. 8, pp. 465–473, Aug. 2008.
[3] R. W. Boyd and D. J. Gauthier, "Controlling the velocity of light pulses," *Science*, vol. 326, no. 5956, pp. 1074–1077, Nov. 2009.
[4] J. Garcia-Ruperez, V. Toccafondo, M. J. Bañuls, J. Garcia Castello, A. Griol, S. Peransi-Llopis, and A. Maqueira, "Label-free antibody detection using band edge fringes in SOI planar photonic crystal waveguides in the slow-light regime," *Opt. Exp.*, vol. 18, no. 23, pp. 24 276–24 286, Nov. 2010.

[5] C. Monat, B. Corcoran, D. Pudo, M. Ebnali-heidari, C. Grillet, M. D. Pelusi, D. J. Moss, B. Eggleton, T. P. White, L. OFaolain, and T. F. Krauss, "Slow light enhanced nonlinear optics in silicon photonic crystal waveguides," *IEEE J. Sel. Topics Quantum Electron.*, vol. 16, no. 1, pp. 344–356, Jan./Feb. 2010.
[6] L. OFaolain, D. M. Beggs, T. P. White, T. Kampfrath, K. Kuipers, and T.F. Krauss, "Compact optical switches and modulators based on dispersion engineered photonic crystals," *IEEE Photon. J.*, vol. 2, no. 3, pp. 404–414, Jun. 2010.
[7] A. Brimont, D. J. Thomson, P. Sanchis, J. Herrera, F. Y. Gardes, J. M. Fedeli, G. T. Reed, and J. Martí, "High speed silicon electro-optical modulators enhanced via slow light propagation," *Opt. Exp.*, vol. 19, no. 1, pp. 20 876–20 885, Oct. 2011.
[8] H. C. Nguyen, Y. Sakai, M. Shinkawa, N. Ishikura, T. Baba, and S. Wire, "10 Gb/s operation of photonic crystal silicon optical modulators," *Opt. Exp.*, vol. 19, no. 14, pp. 13 000–13 007, Jul. 2011.
[9] D. J. Thomson, F. Y. Gardes, J. M. Fedeli, S. Zlatanovic, H. Youfang, B. P. P. Kuo, E. Myslivets, N. Alic, S. Radic, G. Z. Mashanovich, and G. T. Reed, "50-Gb/s silicon optical modulator," *IEEE Photon. Technol. Lett.*, vol. 24, no. 4, pp. 234–236, Jul. 2012.
[10] A. Liu, R. Jones, L. Liao, D. Samara-Rubio, D. Rubin, O. Cohen, R. Nicolaescu, and M. Paniccia, "A high-speed silicon optical modulator based on a metal–oxide–semiconductor capacitor," *Nature*, vol. 427, pp. 615–618, Feb. 2004.
[11] P. Dong, S. Liao, H. Liang, W. Qian, X. Wang, R. Shafiiha, D. Feng, G. Li, X. Zheng, A. V. Krishnamoorthy, and M. Asghari, "High-speed and compact silicon modulator based on a racetrack resonator with a 1 V drive voltage," *Opt. Lett.*, vol. 35, no. 19, pp. 3246–3248, Oct. 2010.
[12] J. C. Rosenberg, W. M. J. Green, S. Assefa, T. Barwicz, M. Yang, S. M. Shank, and Y. A. Vlasov, "Low-power 30 Gbps silicon microring modulator," in *Proc. CLEO*, 2011, pp. 1–2.
[13] X. Xiao, H. Xu, X. Li, Y. Hu, K. Xiong, Z. Li, T. Chu, Y. Yu, and J. Yu, "25 Gb/s silicon microring modulator based on misalignment-tolerant interleaved PN junctions," *Opt. Exp.*, vol. 20, no. 3, pp. 2507–2515, Jan. 2012.
[14] P. Dong, L. Chen, Y.-K. Chen, B. Labs, and H. Road, "High-speed low-voltage single-drive push–pull silicon Mach–Zehnder modulators," *Opt. Exp.*, vol. 20, no. 6, pp. 6163–6169, Mar. 2012.
[15] G. Kim, J. W. Park, I. G. Kim, S. Kim, S. Kim, J. M. Lee, G. S. Park, J. Joo, K.-S. Jang, J. H. Oh, S. A. Kim, J. H. Kim, J. Y. Lee, J. M. Park, D.-W. Kim, D.-K. Jeong, M.-S. Hwang, J.-K. Kim, K.-S. Park, H.-K. Chi, H.-C. Kim, D.-W. Kim, and M. H. Cho, "Low-voltage high-performance silicon photonic devices and photonic integrated circuits operating up to 30 Gb/s," *Opt. Exp.*, vol. 19, no. 27, pp. 26 936–26 947, Dec. 2012.
[16] J. Ding, H. Chen, L. Yang, L. Zhang, R. Ji, Y. Tian, W. Zhu, Y. Lu, P. Zhou, R. Min, and M. Yu, "Ultra-low-power carrier-depletion Mach–Zehnder silicon optical modulator," *Opt. Exp.*, vol. 20, no. 7, pp. 7081–7087, Mar. 2012.
[17] M. Notomi, K. Yamada, A. Shinya, J. Takahashi, C. Takahashi, and I. Yokohama, "Extremely large group-velocity dispersion of line-defect waveguides in photonic crystal slabs," *Phys. Rev. Lett.*, vol. 87, no. 25, pp. 253902-1–253902-4, Dec. 2001.
[18] A. Gomez-Iglesias, D. OBrien, L. OFaolain, A. Miller, and T. F. Krauss, "Direct measurement of the group index of photonic crystal waveguides via Fourier transform spectral interferometry," *Appl. Phys. Lett.*, vol. 90, no. 26, pp. 261107-1–261107-3, Jun. 2007.
[19] H. C. Nguyen, Y. Sakai, M. Shinkawa, N. Ishikura, and T. Baba, "Photonic crystal silicon optical modulators: Carrier-injection and depletion at 10 Gb/s," *IEEE J. Quantum Electron.*, vol. 48, no. 2, pp. 210–220, Feb. 2012.
[20] X. Tu, T. Liow, J. Song, and M. Yu, "Fabrication of low loss and high speed silicon optical modulator using doping compensation method," *Opt. Exp.*, vol. 19, no. 19, pp. 18 029–18 035, Sep. 2011.
[21] F. Y. Gardes, A. Brimont, P. Sanchis, G. Rasigade, D. Marris-Morini, L. O'Faolain, F. Dong, J. M. Fedeli, P. Dumon, L. Vivien, T. F. Krauss, G. T. Reed, and J. Martí, "High-speed modulation of a compact silicon ring resonator based on a reverse-biased pn diode," *Opt. Exp.*, vol. 17, no. 24, pp. 21 986–21 991, Nov. 2009.
[22] A. Brimont, J. Vicente Galán, J. Maria Escalante, J. Martí, and P. Sanchis, "Group-index engineering in silicon corrugated waveguides," *Opt. Lett.*, vol. 35, no. 16, pp. 2708–2710, Aug. 2010.